Evaluation of advection schemes and surface tension model for algebraic and geometric VOF multiphase flow solvers

Simone Di Giorgio [a,c,*], Sergio Pirozzoli [b], Alessandro Iafrati [a]

[a] *Istituto di Ingegneria del Mare, Consiglio Nazionale delle Ricerche (INM-CNR), Via di Vallerano 139, Rome, 00128, Italy*
[b] *Dipartimento di Ingegneria Meccanica e Aerospaziale, Sapienza Università di Roma, via Eudossiana 18, Rome, 00184, Italy*
[c] *Institute of Fluid Mechanics and Heat Transfer, TU-Wien, Getreidemarkt 9, Vienna, 1060, Austria*

ARTICLE INFO

ABSTRACT

This paper addresses the validation and verification of numerical models for complex multiphase flows involving immiscible fluids. Specifically, the focus is on the dynamics of the interface between the fluids, which remains a challenge in many applications. Previous studies have primarily examined simpler flows with limited complexity, while real-world scenarios involve intricate interfaces and turbulent dynamics. To overcome this, a representative test case involving the motion of an oil cube within a water cube proposed by [12] is used. Different computational models using volume-of-fluid (VOF) approaches are validated and compared, with particular attention given to the influence of numerical schemes for convective terms. The impact of these schemes on integral quantities and interface dynamics is analyzed. Particular attention is paid at the surface tension contribution to the energy budgets, which is usually neglected in the available literature. Furthermore, it is shown here that, the model adopted for the surface tension is responsible for an additional contribution to numerical dissipation. To the authors' knowledge, it is the first time that a detailed analysis of such aspects is presented.

1. Introduction

In recent years, significant progress has been made in developing numerical models to simulate multiphase flows and immiscible fluids, with a particular emphasis on their validation and verification. One crucial aspect of these flows is the accurate representation of the interface dynamics between the two fluids. Previous studies validating interface tracking algorithms have often relied on assuming a prescribed and time-varying velocity field [37,33,11]. More comprehensive validation studies have been conducted for multiphase flow solvers that couple the solution of the Navier-Stokes equations with interface tracking/capturing algorithms. These studies involve comparisons with experimental data or theoretical solutions, often of a linear nature [20]. However, in these scenarios, the interface topology is usually not very complex, the flow itself is relatively simple, typically involving a single scale, and the comparisons focus on a limited number of physical aspects. Examples of these aspects include the continuity of stresses across the interface in a two-phase Poiseuille flow [2], the application of the Laplace law to a spherical or circular drop [30], the analysis of oscillation modes of a free surface in the linear regime [32], the head-on coalescence of two drops [1,34], or the Rayleigh-Plateau instability causing the breakup of a low-velocity round jet [7], to name just a few. However, none of these problems consider the

---

presence of a material interface near a turbulent flow involving two-phase dynamics, despite such situations being common in many practical scenarios.

In fact, highly complex multiphase flows are relevant to numerous industrial and environmental problems. To illustrate a few examples, these include the atomization of a liquid jet in an engine [22,23,10], phase separators in chemical engineering processes, ladle-based steel elaboration, boiling crises in nuclear reactors [15], complex bubbly flows such as the flow past Taylor bubbles in pipes [25], droplet or asteroid impacts [21], wave impact on structures, and the widespread phenomenon of wave breaking [6,8]. In most cases, computational approaches need to address the multiscale nature of these flows, especially in environmental and engineering contexts. On one hand, the largest interfacial length scales are associated with structures like jets, films, or massive drops. On the other hand, small interfacial scales emerge from fragmentation processes of bubbles or sprays, leading to the formation of microbubbles or microdroplets and the generation of dissolved aerosols. These two significantly different ranges of interfacial scales interact nonlinearly through processes such as ligament break-up or drop/bubble coalescence. The turbulence or unsteadiness of the carrier fluid motion plays a crucial role in governing these interactions.

One significant challenge lies in defining a benchmark that accurately represents the multiscale sharp interface structures evolving in a turbulent flow. In an effort to address this, Estivalezes et al. [12] proposed an artificial problem as a representative test case where all the typical issues and physical phenomena of multiphase flows come into play. In this problem, a cubic volume of oil initially positioned inside a cube of water moves upward due to the density difference between the two phases. In that reference, multiple multiphase solvers based on both the volume-of-fluid (VOF) approach [19] and the level-set approach [27] were compared, mainly in terms of macroscopic and integral quantities such as potential and kinetic energies, as well as enstrophy. However, a detailed analysis of the influence of the numerical discretization schemes used for the convective terms was not presented.

This study focuses on analyzing the impact of different numerical schemes for the convective terms on integral quantities, such as total energy, kinetic energy, and energy dissipation, as well as the dynamics of the interface between the two phases. The influence of the discretization schemes on the computed solution is herein assessed for both the algebraic and geometric VOF method. Specifically, both the algebraic TVD-VOF (Total Variational Diminishing) scheme as developed by Pirozzoli et al. [29], and the geometric VOF method developed by Weymouth and Yue [36] are considered. Particular attention is paid at estimating the contribution of surface tension to the energy budget, and to highlight errors introduced by the chosen discretization methods.

2. The numerical solver

The computer code solves for the Navier-Stokes solver for an incompressible two-fluids system with density and viscosity varying across their interface. The fluids are assumed to be immiscible, and the interface is implicitly tracked by means of an indicator function χ. The governing equations in nondimensional form are

$$\nabla \cdot \mathbf{u} = 0, \tag{1}$$

$$\frac{\partial \mathbf{u}}{\partial t} + \nabla \cdot (\mathbf{u}\mathbf{u}) = \frac{1}{\rho}\left[-\nabla p + \frac{1}{Re}\nabla \cdot \left(\mu\left(\nabla \mathbf{u} + \nabla \mathbf{u}^T\right)\right) + \frac{1}{We}\mathbf{f}_\sigma\right] - \frac{1}{Fr}\mathbf{j}, \tag{2}$$

$$\frac{\partial \chi}{\partial t} + \mathbf{u} \cdot \nabla \chi = 0, \tag{3}$$

where χ is the phase function, $\mathbf{u} = \mathbf{u}(\mathbf{x},t)$ is the fluid velocity, $p = p(\mathbf{x},t)$ is the pressure, $\rho = \rho(\mathbf{x},t)$ is the density, $\mu = \mu(\mathbf{x},t)$ is the dynamic viscosity, and $\mathbf{j}$ is the unit vector oriented upwards. The surface tension is modelled as a volumetric force concentrate at the interface,

$$\mathbf{f}_\sigma = k\delta\left(\mathbf{x} - \mathbf{x}_s\right)\mathbf{n}, \tag{4}$$

where k is the local curvature of the interface between the two fluids $\mathbf{n}$ is the unit normal of the interface, and δ is the Dirac function which localizes the force at interface points, $\mathbf{x}_s$ [35].

In equation (2), Re, We, and Fr are the Reynolds, Weber, and Froude numbers, respectively, defined as

$$Re = \frac{\tilde{U}\tilde{L}\tilde{\rho}}{\tilde{\mu}}, \quad We = \frac{\tilde{\rho}\tilde{U}^2\tilde{L}}{\sigma}, \quad Fr = \frac{\tilde{U}^2}{g\tilde{L}}, \tag{5}$$

where σ is the surface tension coefficient, g is the gravity acceleration, $\tilde{L}$ and $\tilde{U}$ are the reference values for length and velocity, respectively.

In the VOF (Volume of Fluid) approach the phase function χ accounts for the volume fraction of one of the two phases, and the local density and viscosity are then defined as

$$\rho = \rho_1\chi + (1-\chi)\rho_2, \qquad\qquad \mu = \mu_1\chi + (1-\chi)\mu_2. \tag{6}$$

In this work, equation (3) is discretized by means of both algebraic and geometric VOF. The TVD-VOF method developed by Pirozzoli et al. [29] is considered as a candidate for the algebraic approach, whereas the method proposed by Weymouth and Yue [36] is considered as a candidate for the geometric approach. The Navier-Stokes equations are solved with a classical projection method in which the momentum equation is advanced in time by neglecting the pressure gradient. Hence, the pressure gradient term is determined by enforcing the continuity equation and it is added to the intermediate velocity field in a correction step [4,26]. Time

integration is carried out by means of the Adams–Bashforth explicit scheme for the convective terms and for the off-diagonal part of the viscous terms, and the Crank–Nicolson scheme for the diagonal diffusion terms. Hence, equation (2) becomes in discrete form

$$\frac{\mathbf{u}^{n+1} - \mathbf{u}^n}{\Delta t} = -\frac{1}{\rho^{n+\frac{1}{2}}} \nabla_h p - \left(\frac{3}{2} \mathbf{N}_h^n - \frac{1}{2} \mathbf{N}_h^{n-1}\right) + \frac{1}{2\rho^{n+\frac{1}{2}}} \left(\mathbf{D}_h^n + \mathbf{D}_h^{n+1}\right) + \frac{1}{\rho^{n+\frac{1}{2}}} \mathbf{f}^n , \tag{7}$$

where Δt is the time step. The superscript n denotes quantities evaluated at the beginning of the step and $n+1$ identifies the end of the step. As suggested by Popinet [30], the material properties (viscosity and density) in the previous equation are evaluated by advancing the respective transport equation at staggered times at $n+1/2$. In the above equation $\mathbf{N}_h$ and $\mathbf{D}_h$ denote discretized advective and diffusive terms, respectively, and $\mathbf{f}$ includes both gravity and surface tension forces. Similarly, ∇_h stands for the gradient operator in discrete form. The momentum equation (7) is complemented with the divergence-free conditions,

$$\nabla_h \cdot \mathbf{u}^{n+1} = 0 . \tag{8}$$

The momentum equation (7) is solved in two steps. In the predictor step a preliminary velocity field ($\mathbf{u}^*$) is determined by ignoring the effect of the pressure,

$$\frac{\mathbf{u}^* - \mathbf{u}^n}{\Delta t} = -\left(\frac{3}{2} \mathbf{N}_h^n - \frac{1}{2} \mathbf{N}_h^{n-1}\right) + \frac{1}{2\rho^{n+\frac{1}{2}} Re} \left(\mathbf{D}_h^n + \mathbf{D}_h^*\right) + \frac{1}{\rho^{n+\frac{1}{2}}} \mathbf{f}^n . \tag{9}$$

In the correction step the pressure gradient is added to the preliminary velocity field to yield the velocity field at the new time step,

$$\frac{\mathbf{u}^{n+1} - \mathbf{u}^*}{\Delta t} = -\frac{1}{\rho^{n+\frac{1}{2}}} \nabla_h p . \tag{10}$$

The sum of equations (9) and (10) yields exactly equation (7). By taking the divergence of equation (10) and using equation (8) to eliminate $\mathbf{u}^{n+1}$, a variable-coefficients Poisson equation for the pressure is obtained

$$\nabla_h \cdot \left(\frac{1}{\rho^{n+\frac{1}{2}}} \nabla_h p\right) = \frac{1}{\Delta t} \nabla_h \cdot \mathbf{u}^* , \tag{11}$$

whose solution yields the pressure, and thus the updated velocity field via equation (10).

The convective terms and the off-diagonal part of the viscous operator are rearranged as

$$\begin{aligned}
\mathbf{N}_h^n &= \nabla_h \cdot \mathbf{u}^n \mathbf{u}^n - \frac{1}{\rho^{n+\frac{1}{2}} Re} \nabla_h \cdot \left(\mu^{n+\frac{1}{2}} \nabla \mathbf{u}^{Tn}\right), \\
\mathbf{N}_h^{n-1} &= \nabla_h \cdot \mathbf{u}^{n-1} \mathbf{u}^{n-1} - \frac{1}{\rho^{n+\frac{1}{2}} Re} \nabla_h \cdot \left(\mu^{n+\frac{1}{2}} \nabla \mathbf{u}^{Tn-1}\right) ,
\end{aligned} \tag{12}$$

whereas the diagonal part of the viscous term becomes

$$\mathbf{D}_h^n = \nabla_h \cdot \left(\mu^{n+\frac{1}{2}} \nabla \mathbf{u}^n\right), \qquad \mathbf{D}_h^* = \nabla_h \cdot \left(\mu^{n+\frac{1}{2}} \nabla \mathbf{u}^*\right) , \tag{13}$$

which, by defining $\delta \mathbf{u}^n = \mathbf{u}^* - \mathbf{u}^n$, allows to reformulate the problem in *delta* form,

$$\mathbf{D}_h^n + \mathbf{D}_h^* = \nabla_h \cdot \left(\mu^{n+\frac{1}{2}} \left(\nabla_h \mathbf{u}^n + \nabla_h (\delta \mathbf{u}^n + \mathbf{u}^n)\right)\right) = \nabla_h \cdot \left(\mu^{n+\frac{1}{2}} \left(\nabla_h \delta \mathbf{u}^n + 2 \left(\nabla_h \mathbf{u}^n\right)\right)\right) . \tag{14}$$

Starting from equation (9), it follows that

$$\frac{\delta \mathbf{u}^n}{\Delta t} - \frac{1}{2\rho^{n+\frac{1}{2}} Re} \nabla_h \cdot \left(\mu^{n+\frac{1}{2}} \nabla_h \delta \mathbf{u}^n\right) = -\left(\frac{3}{2} \mathbf{N}_h^n - \frac{1}{2} \mathbf{N}_h^{n-1}\right) + \frac{1}{\rho^{n+\frac{1}{2}} Re} \mathbf{D}_h^n + \frac{1}{\rho^{n+\frac{1}{2}} We} \mathbf{f}_\sigma^n - \frac{1}{Fr} \mathbf{j} . \tag{15}$$

The left-hand side of the above equation is discretized using second-order finite differences, and the right-hand side is denoted as RHS_i, where i is the i-th component, thus yielding

$$\left[1 - \Delta t \left(L_{i1} - L_{i2} - L_{i3}\right)\right] \delta u_i = RHS_i . \tag{16}$$

The above equation is then solved through approximate factorization, namely

$$\left(1 - A_{i1}\right) \left(1 - A_{i2}\right) \left(1 - A_{i3}\right) \delta u_i = RHS_i, \tag{17}$$

where $A_{ij} = \Delta t L_{ij}$, and

$$\begin{aligned}
A_{i1} &= \frac{1}{2\rho^{n+\frac{1}{2}}} \frac{\partial}{\partial x_1} \left(\mu^{n+\frac{1}{2}} \frac{\partial}{\partial x_1}\right), \\
A_{i2} &= \frac{1}{2\rho^{n+\frac{1}{2}}} \frac{\partial}{\partial x_2} \left(\mu^{n+\frac{1}{2}} \frac{\partial}{\partial x_2}\right), \\
A_{i3} &= \frac{1}{2\rho^{n+\frac{1}{2}}} \frac{\partial}{\partial x_3} \left(\mu^{n+\frac{1}{2}} \frac{\partial}{\partial x_3}\right).
\end{aligned} \tag{18}$$

The left-hand-side of equation (17) can be shown to be a third-order accurate approximation of the large sparse matrix at the left-hand-side of equation (16) [26]. Equation (17) can then be solved by sequential application of tridiagonal equations solvers,

$$
\begin{aligned}
\left(1 - A_{i1}\right) \delta u_i^{**} &= RHS_i, \\
\left(1 - A_{i3}\right) \delta u_i^{*} &= \delta u_i^{**}, \\
\left(1 - A_{i2}\right) \delta u_i^{n} &= \delta u_i^{*} ,
\end{aligned}
\tag{19}
$$

where δu^{**} and δu^{*} denote time increments at fictitious intermediate stages.

The solution of the Poisson equation (11) for the corrective pressure is the most expensive part of the algorithm, as it should be carried out with iterative methods. In this respect, the algorithms in the HYPRE library [13] are found to be quite efficient in massively parallel computations. Either geometric multigrid and Krylov methods have been tested, the latter resulting to be more robust in the presence of complicated interface topologies.

2.1. Spatial discretization

The momentum equations are discretized in the finite-difference framework with a staggered grid layout, where the pressure, the phase function and the material properties are defined at the cell centers, whereas the velocity components are stored at the middle of the cell faces [17]. The right-hand-side (**RHS**) of equation (15), is rewritten in order to cast convective and diffusive terms in a more canonical form,

$$
\begin{aligned}
\mathbf{RHS} \quad &= -\left(\tfrac{3}{2}\mathbf{H}_h^n - \tfrac{1}{2}\mathbf{H}_h^{n-1}\right) + \frac{1}{\rho^{n+\frac{1}{2}} Re}\left[\boldsymbol{\Sigma}_h^n + \tfrac{1}{2}\left(\nabla_h \mathbf{u}^{Tn} - \nabla_h \mathbf{u}^{Tn-1}\right)\nabla_h \mu^{n+\frac{1}{2}}\right] \\
&\quad + \frac{1}{\rho^{n+\frac{1}{2}} We}\mathbf{f}_\sigma^n - \frac{1}{\rho^{n+\frac{1}{2}} Fr}\mathbf{j} ,
\end{aligned}
\tag{20}
$$

where $\mathbf{H}_h$ and $\boldsymbol{\Sigma}_h$ denote, respectively, convective and viscous terms. Terms associated with variation of viscosity appear in this case, which are rearranged as

$$
\frac{1}{\rho^{n+\frac{1}{2}} Re}\left[\frac{3}{2}\nabla_h \cdot \left(\mu^{n+\frac{1}{2}}\nabla\mathbf{u}^{Tn}\right) - \frac{1}{2}\nabla_h\left(\mu^{n+\frac{1}{2}}\nabla\mathbf{u}^{Tn-1}\right)\right] =
$$
$$
\frac{1}{\rho^{n+\frac{1}{2}} Re}\left[\nabla_h \cdot \left(\mu^{n+\frac{1}{2}}\nabla\mathbf{u}^{Tn}\right) + \frac{1}{2}\left(\nabla_h \cdot \left(\mu^{n+\frac{1}{2}}\nabla\mathbf{u}^{Tn}\right) - \nabla_h \cdot \left(\mu^{n+\frac{1}{2}}\nabla\mathbf{u}^{Tn-1}\right)\right)\right] , \tag{21}
$$

and exploiting incompressibility one obtains

$$
\nabla_h \cdot \left(\mu^{n+\frac{1}{2}}\nabla\mathbf{u}^{Tn}\right) = \nabla_h\mathbf{u}^{Tn}\nabla_h\mu^{n+\frac{1}{2}} + \mu^{n+\frac{1}{2}}\nabla_h \cdot \nabla_h\mathbf{u}^{Tn} = \nabla_h\mathbf{u}^{Tn}\nabla_h\mu^{n+\frac{1}{2}} + \mu^{n+\frac{1}{2}}\nabla_h\left(\nabla_h \cdot \mathbf{u}\right) = \nabla_h\mathbf{u}^{Tn}\nabla_h\mu^{n+\frac{1}{2}} . \tag{22}
$$

As for the convective terms, defined as

$$
\mathbf{H}_h^n = \nabla_h \cdot (\mathbf{u}^n\mathbf{u}^n), \qquad \mathbf{H}_h^{n-1} = \nabla_h \cdot \left(\mathbf{u}^{n-1}\mathbf{u}^{n-1}\right) , \tag{23}
$$

a centered second-order discretization is used (e.g., [17,26]), which is generally best suitable for fully resolved single-phase flows, yielding discrete preservation of the total kinetic energy. For the diffusive terms, which are written as

$$
\boldsymbol{\Sigma}_h^n = \nabla_h \cdot \mu^{n+\frac{1}{2}}\left(\nabla_h\mathbf{u}^n + \nabla_h\mathbf{u}^{Tn}\right), \tag{24}
$$

a standard second-order central discretization is used [35].

2.2. Surface tension

In this work the continuum surface force method (CSF) [3], is used to determine the equivalent local body force to model surface tension. In particular, the Dirac delta function $\delta_s = \delta\left(\mathbf{x} - \mathbf{x}_s\right)$, used in Eq. (4), is approximated as $\left|\nabla_h\chi\right|$ and since the interface normal is $\mathbf{n} = -\nabla_h\chi / \left|\nabla_h\chi\right|$, the surface tension is rearranged to the following form

$$
\mathbf{f}_\sigma = -k\nabla_h\chi , \tag{25}
$$

where the interface curvature is evaluated through the height function method [5,14,18,24,30], which is known to work well as long as the height function is within the cell dimension [5]. At points where this condition is not met, the curvature estimation based on the gradient of the interface normal vector [16] is adopted, hence

$$
k = \frac{\nabla\tilde{\chi} * H(\tilde{\chi}) * \nabla\tilde{\chi}^T - |\nabla\tilde{\chi}|^2 \mathrm{tr}\left(H(\tilde{\chi})\right)}{2|\nabla\tilde{\chi}|^3}, \tag{26}
$$

where $\nabla\tilde{\chi}$ and $H(\tilde{\chi})$ are, respectively, the gradient and the Hessian of the smoothed phase function. The first- and second-order derivative of the phase function field are approximated by using the least-square method [9]. A detailed verification and validation study of the surface tension model adopted here is provided in Di Giorgio et al. [8].
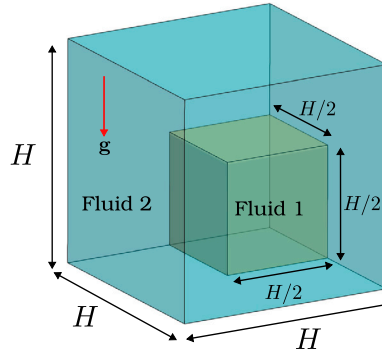
Fig. 1. Initial setup of the phase-inversion problem in a closed box. The light liquid or oil is fluid 1 and the denser, less viscous liquid is fluid 2.

2.3. Discretization of advective terms

As for the advective terms ($\mathbf{H}_h = \nabla_h \cdot (\mathbf{uu})$) two options are considered, namely a centered second-order scheme (MAC) with energy-preserving properties, and a more robust second-order upwind-biased TVD scheme. The two schemes can be used either independently or in combined fashion. In the latter case, a simple "interface sensor" is introduced,

$$\phi_i = \left| \chi_{i+1/2} - \chi_{i-1/2} \right| , \tag{27}$$

such that it is zero inside each phase, and it is different than zero (however, less than one), around interfaces.

In a one-dimensional setting, the convective terms of momentum equation (23) become

$$H_i = \frac{1}{\Delta x} \left(f_{i+1/2} - f_{i-1/2} \right), \tag{28}$$

where f is the numerical flux. Now let

$$f_{i+1/2}^{MAC} = \left(\frac{u_{i+1} + u_i}{2} \right)^2 , \tag{29}$$

be the numerical flux for the second-order MAC scheme, and

$$f_{i+1/2}^{TVD} = \begin{cases} \left(u_i + \frac{1}{2} \delta u_i \varphi(\theta_i) \right)^2 & \text{if} \quad \frac{1}{2} \left(u_{i+1} + u_i \right) > 0, \\ \left(u_{i+1} - \frac{1}{2} \delta u_i \varphi(\theta_{i+1}) \right)^2 & \text{if} \quad \frac{1}{2} \left(u_{i+1} + u_i \right) \leq 0, \end{cases} \tag{30}$$

be the numerical flux for the TVD scheme, where $\delta u_u = u_{i+1} - u_i$, $\theta_i = \delta u_{i+1}/\delta u_i$, and the minmod limiter is selected,

$$\varphi(\theta) = \max \left(0, \min \left(\theta, 1 \right) \right). \tag{31}$$

The two numerical fluxes can be also combined together as

$$f_{i+1/2} = f_{i+1/2}^{MAC} + \phi_i \left(f_{i+1/2}^{TVD} - f_{i+1/2}^{MAC} \right), \tag{32}$$

with ϕ_i defined in equation (27). The numerical flux (32) guarantees use of the energy-conserving MAC flux in single-phase regions, while restricting use of the TVD numerical dissipation to the surroundings of the fluids interface. This is especially appropriate as very often in multiphase flow simulations, the regions about the interface are not adequately resolved due to fragmentation processes, hence use of central schemes may induce nonphysical oscillations, which numerical dissipation effectively suppresses. This hybrid approach (hereafter referred to as HYB scheme) is also more computationally effective, as the computationally cheaper MAC scheme is applied to the vast majority of fluid points.

3. Case set-up and validation

To validate the numerical model, a benchmark test case is undertaken. This test case involves a cubic blob of a light liquid, denoted as fluid 1, initially positioned at the bottom of a cubic box filled with a heavier liquid, referred to as fluid 2, as illustrated in Fig. 1. The cubic box has dimensions (H, H, H), and the light fluid blob occupies one corner, having dimensions $(H/2, H/2, H/2)$. To model the behavior at the boundaries, all the outer walls are considered as free-slip impermeable walls. This means that the normal velocity is set to zero, and the tangential components satisfy a symmetry condition, ensuring shear-free behavior. As for the volume fraction boundary condition, a 90° static contact angle at the walls is imposed. This is achieved by enforcing the wall-normal derivative of the volume fraction χ to be zero at the boundary. The gravitational acceleration is set to $\mathbf{g} = (0, -9.81, 0)[m/s^2]$, the surface tension coefficient is $\sigma = 0.045[N/m]$, and the remaining fluid properties are provided in Table 1.

Table 1
Physical properties of the two fluids for the flow cases under study.

Flow case	$\rho_1 \, [Kg/m^3]$	$\rho_2 \, [Kg/m^3]$	$\mu_1 \, [Pa \cdot s]$	$\mu_2 \, [Pa \cdot s]$	Re	We
FC1	900	1000	–	–	–	–
FC2	900	1000	0.1	0.001	1.37×10^4	41.6

Table 2
List of computational set-ups under scrutiny.

Acronym	Interface transport model	Discretization of convective terms
A-MAC:	Algebraic VOF	Energy-preserving (MAC)
A-TVD:	Algebraic VOF	TVD-MinMod
A-HYB:	Algebraic VOF	Hybrid MAC-TVD
G-MAC:	Geometric VOF	Energy-preserving (MAC)
G-TVD:	Geometric VOF	TVD-MinMod scheme
G-HYB:	Geometric VOF	Hybrid MAC-TVD

To facilitate comparisons with other studies, it is beneficial to define non-dimensional parameters for the problem, namely the Reynolds number (Re) and the Weber number (We), which are expressed as follows

$$Re = \frac{\rho_2 H U_K}{\mu_2}, \quad We = \frac{\rho_2 H U_K^2}{\sigma}, \tag{33}$$

where $H = 0.1 \, [m]$ is the characteristic length scale of the problem, and U_K is a representative upper-bound velocity, defined as Estivalezes et al. [12]

$$U_K = \frac{\sqrt{11}}{8} \sqrt{\frac{\rho_2 - \rho_1}{\rho_1} g H}. \tag{34}$$

Two distinct flow cases were carried out to investigate the performance of different discretizations of the convective terms, and the role played by the interface sensor. In Flow Case 1, the rise of the oil box was simulated by neglecting the viscous and surface tension terms, thus effectively solving the Euler equation. This setup allows to quantify the artificial dissipation of the scheme and, more importantly, to characterize the behavior of different discretization approaches for the convective terms. In contrast, Flow Case 2 incorporates all terms from the Navier-Stokes equations, providing insights into the impact of the numerical scheme on the dynamics of the interface. For both flow cases, the time step was chosen to satisfy the CFL (Courant-Friedrichs-Lewy) condition, specifically set to $CFL = 0.25$. The baseline spatial discretization relies on a uniform grid with $N = 32^3$ nodes, resulting in a grid size of $\Delta/H = 0.03125$, hence coarser than the reference study of Estivalezes et al. [12]. The Kolmogorov length scale ($\eta_k = Re^{-3/4} H$) and the Hinze length scale ($\eta_H = We^{-3/5} H$) for Flow Case 2 are estimated by using Re and We defined in eq. (33), to be $\eta_k/H = 7.9 \cdot 10^{-4}$ and $\eta_H/H = 0.107$, respectively. Hence, the baseline 32^3 mesh suffices to resolve Hinze scale, whereas the Kolmogorov scale is largely under-resolved. Finer meshes have then been considered in a grid refinement study, reported in Section 6.

Numerical simulations of Flow Cases 1 and 2 have been conducted by using various discretizations of the convective terms, as well as interface advection schemes, as illustrated in Table 2. In particular, both algebraic (A), and geometric (G) interface tracking methods have been considered, along with various discretization schemes of the convective terms: purely central, energy-preserving scheme, purely upwind scheme (TVD), and a hybrid version of the two, controlled by the interface sensor (HYB). These simulations allow for a comprehensive investigation of the impact of the various numerical schemes on the predicted behavior of the fluid system. The goal is to analyze how each combination performs in terms of accuracy, stability, and preservation of energy and other key properties.

The comparison of the results obtained using different numerical setups is conducted based on several global physical quantities, including the mass-conservation error, the total energy of the system, and the total viscous dissipation. The mass-conservation error (M_{err}) is defined as the variation of the total mass with respect to its initial value, namely

$$M_{err} = \left| 1 - \frac{M_{tot}}{M_0} \right| \times 100, \tag{35}$$

where M_{tot} is the total mass given by

$$M_{tot} = \int_V \left(\rho_1 \chi + (1 - \chi)\rho_2 \right) dV, \tag{36}$$

and M_0 is the total mass at the initial time. The mass-conservation error of the j-th fluid is defined as:

$$M_{j_{err}} = \left(\frac{M_{j_0} - M_j}{M_0} \right) \times 100, \quad j = 1, 2 \tag{37}$$

where

$$M_1 = \int_V \chi \left(\rho_1 \chi + (1 - \chi) \rho_2 \right) \mathrm{d}V, \quad M_2 = \int_V (1 - \chi) \left(\rho_1 \chi + (1 - \chi) \rho_2 \right) \mathrm{d}V, \tag{38}$$

and M_{j_0} is the mass of the j-th fluid at the initial time. The total energy of the system (E_{tot}) is defined as the sum of kinetic energy (E_K) and potential energy (E_P) and can be expressed as follows

$$E_{tot} = \underbrace{\int_V \frac{1}{2} \rho \left(u^2 + v^2 + w^2 \right) \mathrm{d}V}_{E_K} + \underbrace{\int_V \rho g y \, \mathrm{d}V}_{E_P}, \tag{39}$$

where E_K denotes the total kinetic energy, and E_P denotes the total potential energy. The contribution of energy content associated with surface tension effects is neglected in this definition. Last, the total dissipation associated with viscous effects (ϵ) is defined as

$$\epsilon = \int_V \nabla \cdot \mu \left(\nabla \mathbf{u} + \nabla \mathbf{u}^T \right) : \nabla \mathbf{u} \, \mathrm{d}V, \tag{40}$$

which quantifies the conversion of mechanical energy into heat due to viscous effects. By evaluating these physical quantities for each simulation with different numerical schemes, a comprehensive comparison of their performance can be outlined. In particular, based on the above equations, the artificial dissipation at a given time t is evaluated in non-dimensional form as follows:

$$E_a(t) = \frac{1}{E_{tot}(0)} \left(\left[E_{tot}(0) - E_{tot}(t) \right] - \int_0^t \epsilon(\tau) \, \mathrm{d}\tau \right). \tag{41}$$

4. Flow Case 1: inviscid flow, no surface tension

To assess the impact of different numerical schemes for the discretization of the convective terms on numerical dissipation, simulations are initially carried out by discarding viscous and surface tension effects. Under these conditions the total energy should in principle be conserved since there are no physical dissipation terms in the governing equations. However, without surface tension effects the two fluids can mix freely, and density is no longer a material property. It means that the numerical model based on the VOF approach, which assumes a sharp interface between the two fluids, and without any diffusion term for the density, cannot capture the flow dynamics accurately. Hence, while this artificial setup provides valuable insights into the numerical dissipation characteristics of different schemes for convective term discretization, and allows to isolate the role played by the model adopted for surface tension, it is important to bear in mind its intrinsic limitations and their potential impact on solutions obtained in real-world scenarios involving fluid mixing and diffusion.

In Fig. 2a, the time histories of the mass-conservation error and of the energy content are presented, each scaled by its initial value. The results demonstrate that the variation of the total mass is consistently very small, reaching at most a fraction of the order of 10^{-5} times the initial mass. However, notable differences arise associated with both the interface tracking method and the schemes used for the discretization of the convective terms. This effect is particularly apparent in the case of the geometric VOF method, for which use of the TVD scheme or the HYB scheme significantly improves mass conservation as compared to the MAC scheme. Very similar trends of the total mass are observed when comparing the results with those obtained by the reference open-source solver Basilisk [31], based on the geometric VOF and TVD discretization, thus proving the reliability of the present solver. In addition in Fig. 2b the mass-conservation of the two fluids are reported separately, it is worth noticing that the variation of the mass of the individual fluids is much higher than the variation of the overall mass, and, here the algebraic VOF exhibits larger errors in comparison to geometric VOF.

Regarding the total energy, reported in Fig. 2c, the results obtained using the MAC scheme in combination with algebraic VOF show nearly perfect conservation. In all other cases, variations in the total energy content up to about 2% are found. The same also happens when the MAC scheme is combined with geometric VOF, although the variation of the total energy at the end of the simulation is less than half of that obtained when using other schemes. By comparing the energy losses obtained with the same VOF method, it is clear that simulations carried out with the TVD scheme display the highest dissipation, followed by the HYB scheme, whereas those carried out with the MAC scheme show least dissipation. The difference in the energy losses is due to the different approximations of the convective terms, and in particular to the use of upwind-biased TVD discretizations [28].

A better understanding of the solutions can be achieved by looking at the kinetic and potential energy components, which are provided in Fig. 2d, The Potential energy is drawn by subtracting the initial value so that it can be compared to kinetic energy on the same graph. The initial configuration, with the lighter fluid is at the bottom corner, is unstable and, as soon as the simulation is initiated, gravity pushes the lighter fluid upwards and the heavier fluid downwards. This motion leads to a reduction of the potential energy, which is converted into kinetic energy. The system then reaches a minimum of the potential energy, corresponding to a maximum of the kinetic energy. When the lighter fluid touches the upper boundary, it rebounds and its momentum gradually diminishes, while the potential energy approaches a constant value. The constant value is higher for the algebraic VOF approach, particularly when the MAC or HYB schemes are used which give a potential energy about 0.6% higher than the other methods. The results obtained with the geometric VOF are generally in line with the Basilisk solver. Being the fluids inviscid, the small-scale motion activated by gravity should not be damped out, and that is indeed the case for the MAC scheme for both algebraic and geometric
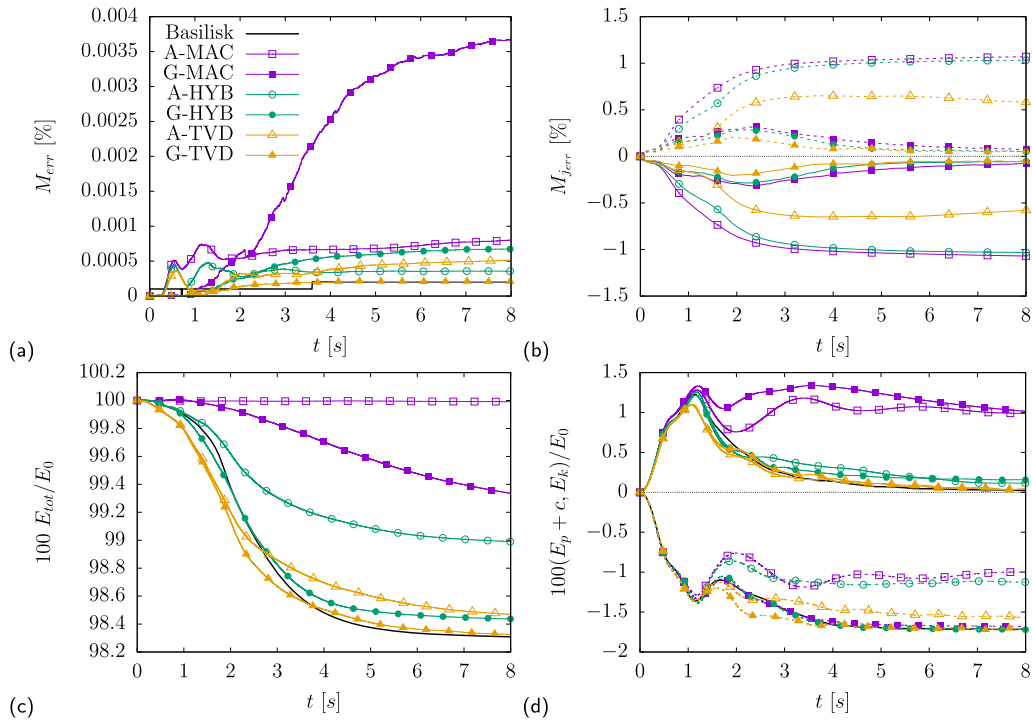
Fig. 2. Comparison of total mass-conservation error (a), mass conservation error for fluid 1 (oil, solid line) and fluid 2 (water, dashed line) (b), total energy (c), kinetic energy (solid line), and potential energy (dashed line) (d) versus time for FC1 simulations (inviscid flow, no surface tension) using algebraic VOF (open symbols), and geometric VOF (filled symbols) with MAC scheme (purple line), TVD scheme (yellow line) and HYB scheme (green line). Reference results obtained with the Basilisk solver are shown with black lines. (For interpretation of the colors in the figure(s), the reader is referred to the web version of this article.)

VOF, which predict about 1% of the initial energy content remaining in the form of kinetic energy. In all other approaches kinetic energy goes back to zero as a consequence of the artificial dissipation induced by the numerical scheme and by the interface tracking algorithm. In particular, the TVD scheme is most dissipative, and its results are in line with the Basilisk solver.

The above results clearly highlight the extremely low level of artificial dissipation of the MAC scheme, in particular when used in combination with the algebraic VOF, compared to the other. The HYB scheme offers a good compromise keeping the robustness of the TVD scheme in terms of stability but, confining the use of dissipative schemes to a narrow region, yields better performance in terms of energy conservation compared to the TVD approach.

In Fig. 3, solutions at time $t = 1$ [s] of FC1 simulations are presented in terms of the volume fraction and interface. The volume fractions are displayed on the bottom plane and on the two side planes of the box, and the interface is visualized as the $C = 0.5$ iso-surface of the volume fraction. At the top of the figure the results obtained with Basilisk are shown as a reference solution, whereas the two rows below display solutions obtained with the algebraic and geometric VOF methods. In each row, from left to right, the solutions obtained using the MAC scheme, the HYB scheme and the TVD scheme are displayed. Although characterized by some common features, remarkable differences can be noted in terms of interface shape and topology, which suggest that both the interface tracking algorithm and the discretization scheme of the convective terms significantly affect the behavior of the interface. When using the algebraic VOF method, the volume fraction gets smeared out, and this phenomenon is particularly evident when the MAC scheme is used (see Fig. 3b). Diffusion of the interface is significantly reduced when TVD schemes are used, although they introduce artificial dissipation. It is worth noting that diffusion of the interface does not imply mass loss, as shown in Fig. 2a. When the geometric VOF method is used, the interface remains much sharper, but energy conservation is significantly worse, as previously discussed and shown in Fig. 2b. The use of the TVD scheme (see Fig. 3d, g) yields similar interface configurations for both interface advection methods, confirming that the use of the TVD scheme for the convective terms, although introducing artificial dissipation, helps retaining sharpness of the density distribution. A much smoother interface is also observed, which is connected with increased numerical dissipation.

In Fig. 4, snapshots of numerical solutions at the final time ($t = 8$ [s]) are shown. At this time the flow has reached a quasi-steady state, with some residual motion. Rather remarkable differences are observed between the results obtained with the algebraic and geometric VOF when the MAC or the HYB schemes are employed. The results shown in Fig. 4b, c, d, corresponding to simulations with algebraic VOF, indicate that the interface remains sharp only if the TVD scheme is used, while the MAC or the HYB schemes are unable to preserve sharpness of the interface. It is worth noting that, although formally the VOF method is used to model the density as a material property, when the algebraic approach is used, the MAC and the HYB schemes introduce significant smearing of the density jump, hence the $C = 0.5$ iso-surface marking the interface between the two fluids, is lost over time. This is of course an artifact of the interface advection scheme but, as explained above, in absence of surface tension it mimics to some
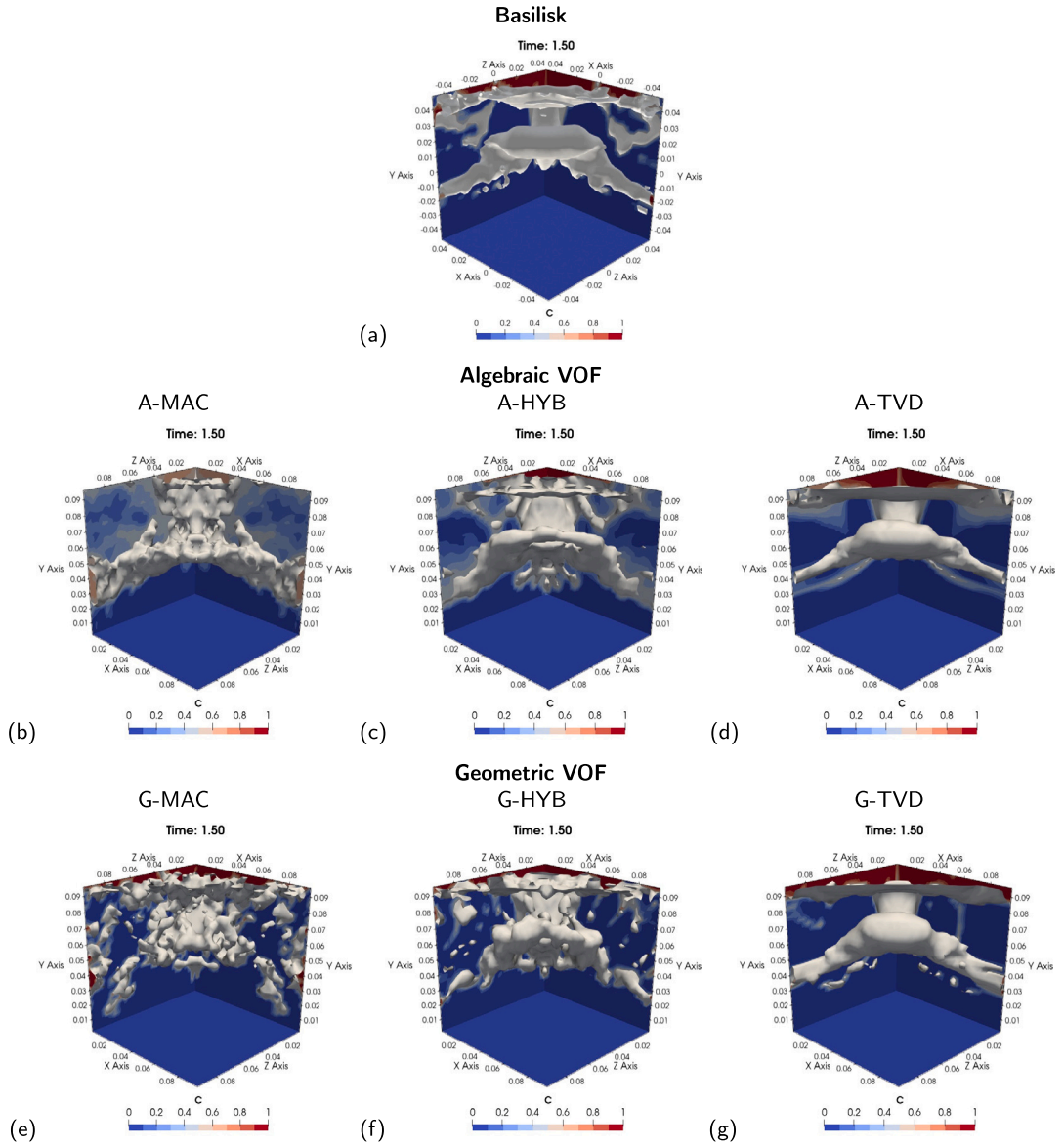
Fig. 3. Flow Case 1: numerical results at $t = 1.5$ [s], obtained by using algebraic (b, c, d) and geometric (e, f, g) VOF with different discretization schemes of convective terms: MAC (b, e), HYB (c, f), TVD (d, g), and Basilisk solver (a). Colored contours of the volume fraction (C) are shown in the coordinate planes, and the $C = 0.5$ iso-surface is shown in grey.

extent the complete miscibility of the two fluids, in that the density of fluid particles varies in time as a result of artificial smearing of the density jump. Complete mixing of the two fluids would yield an average density of $987.5[kg/m^3]$, which is above the value $950[kg/m^3]$ corresponding to the $C = 0.5$ value of the VOF function used to identify the interface between the two fluids, which explains why the iso-surface is not visible in Fig. 4b, and c.

When the geometric VOF is used for tracking (Fig. 4e, f, g), the interface remains sharp, regardless of the advection scheme in use. In the geometric VOF scheme, the segments used to define the interface act as a sort of impermeable surface that prevents smearing of the density field and thus mixing of the two fluids. Therefore, the final solution is in all cases characterized by the lighter fluid lying at the top. As shown in Fig. 2c and d, when using the MAC scheme, the kinetic energy obtained with the geometric VOF is about the same as that obtained with the algebraic model, whereas the potential energy is about 0.6% less, because the lighter fluid is at the top. In this regard, the difference in the total energy observed in Fig. 2b between algebraic and geometric VOF computed with the MAC scheme is mainly associated with the difference in the potential energy. Since, based on the assumptions made in FC1, the total energy should be conserved, the difference in the potential energy of the geometric VOF should be converted into kinetic energy, which should then be higher than for the algebraic model. This means that, although from Fig. 2c the kinetic energy is about the same as for the algebraic model, geometric VOF introduces some artificial dissipation.
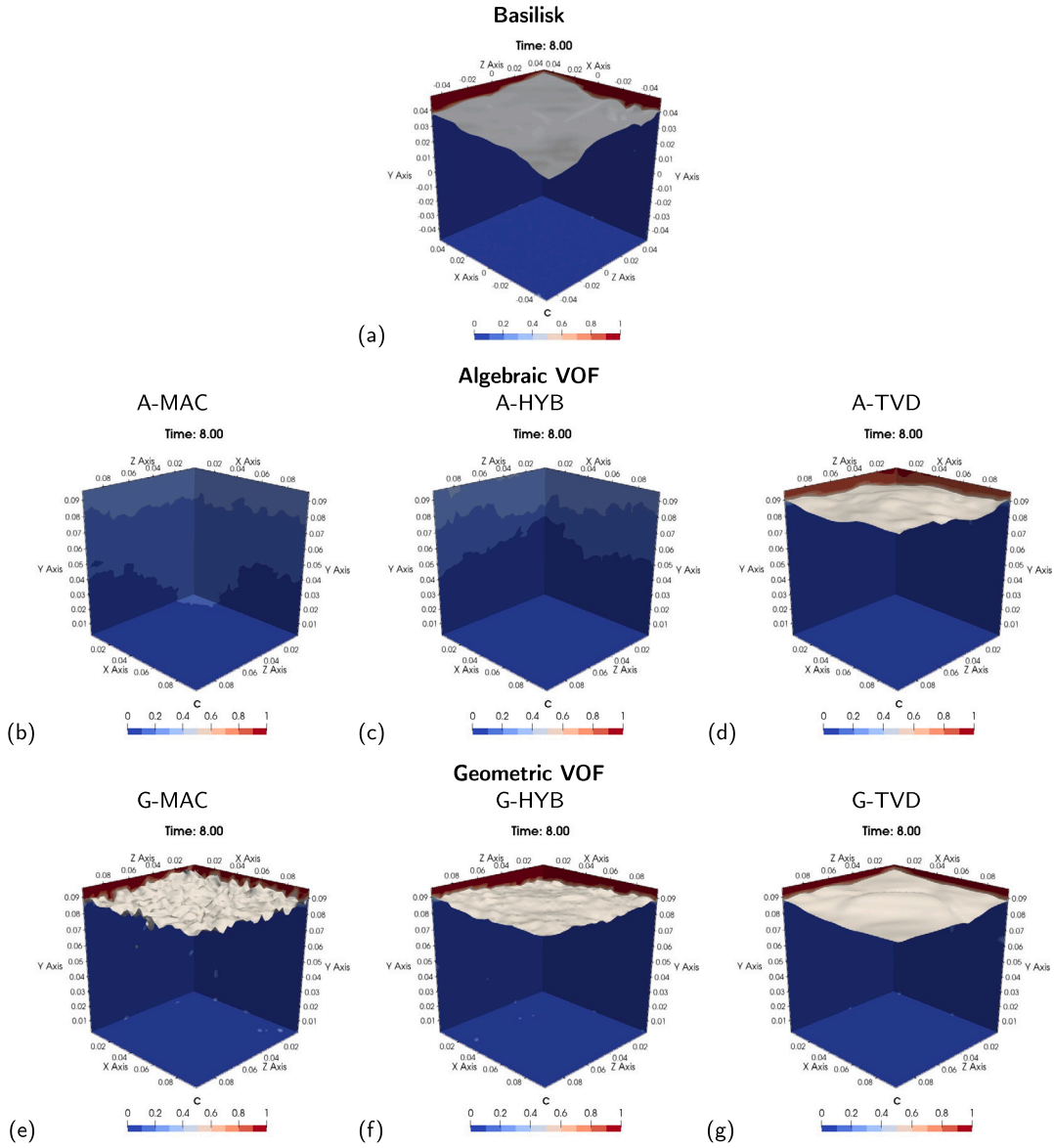
Fig. 4. Flow Case 1: numerical results at $t = 8$ [s], obtained by using algebraic (b, c, d) and geometric (e, f, g) VOF with different discretization schemes of convective terms: MAC (b, e), HYB (c, f), TVD (d, g), and Basilisk solver (a). Colored contours of the volume fraction (C) are shown in the coordinate planes, and the $C = 0.5$ iso-surface is shown in grey.

By comparing the configurations obtained with the geometric VOF for the different advection schemes, one can notice the MAC scheme yields a rather bumpy interface, which is a consequence of the undamped motion of the fluid and of the residual kinetic energy content, as previously discussed. A much smoother interface is obtained when using the HYB scheme, and even more with the TVD scheme, due to artificial damping of the residual velocity field. The best results in terms of energy conservation are obtained when the geometric VOF is used in combination with the MAC scheme, whereas the HYB and the TVD schemes are responsible for extra 1% artificial dissipation.

In summary, FC1 is a test case designed to investigate the capabilities of the numerical schemes to preserve the energy and to correctly describe the interface dynamics. As observed, in the absence of surface tension the fluids can mix, hence the VOF method, developed to model immiscible fluids with an interface, conveys inherent approximations. It is found that the MAC scheme is definitely superior in terms of reduced artificial dissipation regardless of the approach used to track the interface dynamics, whereas the TVD scheme, although improving on robustness, introduces a substantial amount of artificial dissipation. The HYB scheme is somewhat better than the TVD in terms of energy conservation. Regarding with the model adopted for the advection of the VOF function, the algebraic approach, when combined with the MAC or with the HYB schemes, cannot retain the sharpness of the interface. The spurious smearing of the density jump that to some extent mimics the mixing of the fluids, yields better conservation
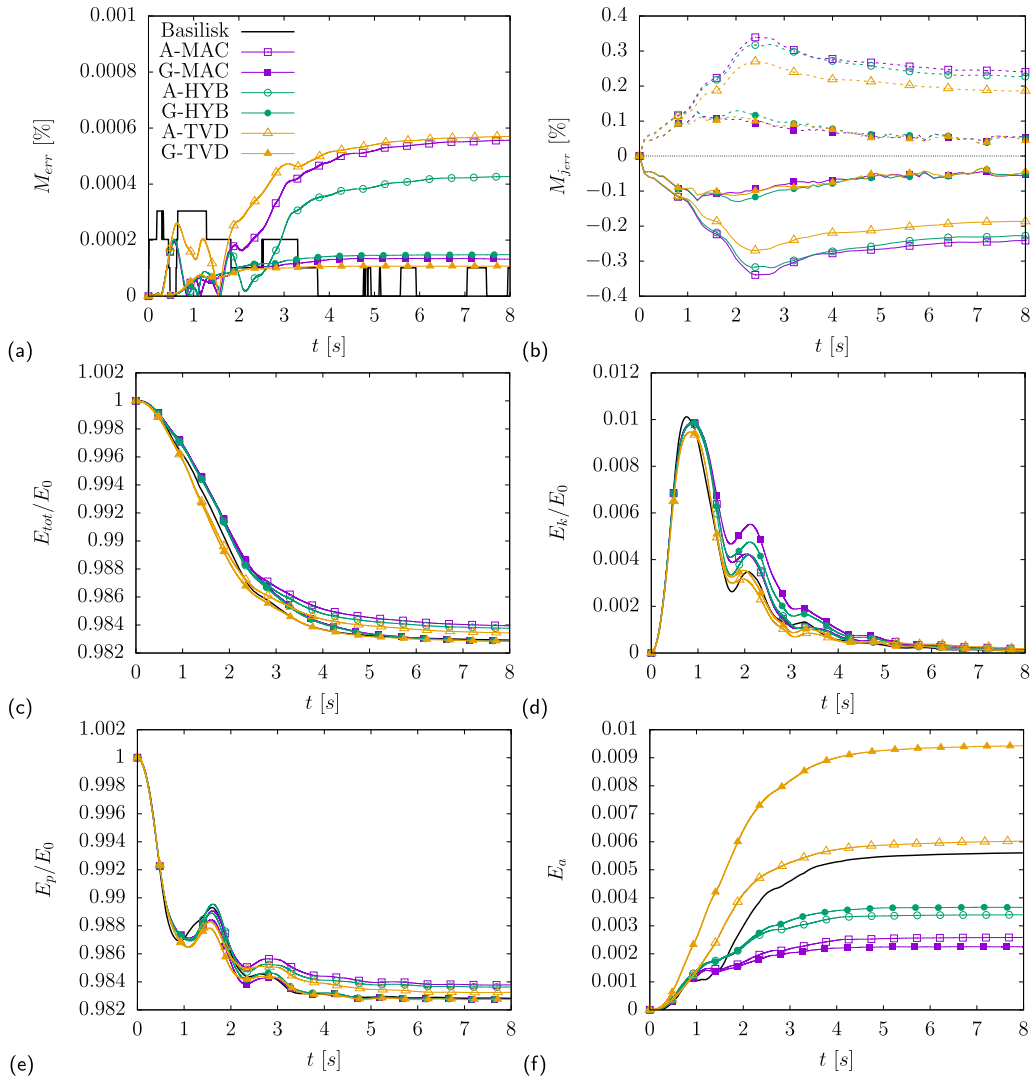
Fig. 5. Comparison of total mass-conservation error (a), mass conservation error for fluid 1 (oil, solid line) and fluid 2 (water, dashed line) (b), total energy (c), kinetic energy (d), potential energy (c), and artificial dissipation (d) versus time for FC2 simulations (viscous flow); using algebraic VOF (open symbols), and geometric VOF (filled symbols) with MAC scheme (purple line), TVD scheme (yellow line) and HYB scheme (green line). Reference results obtained with the Basilisk solver are shown with black lines.

of the total energy. The geometric VOF, being able to preserve the sharpness of the density jump and thus the separation between the two fluids, predicts in all cases the lighter fluid lying at the top, thus allowing an additional amount of potential energy to be converted into kinetic energy. However, even using the MAC scheme, this extra amount is lost due to numerical dissipation. The numerical dissipation is much higher when the HYB or TVD schemes are used.

5. Flow Case 2: viscous two-phase flow with surface tension

The FC2 simulations address the full set of the Navier-Stokes equations, including viscous terms and surface tension effects. The associated time histories of the mass-conservation error, total energy, kinetic energy, potential energy and artificial dissipation are presented in Fig. 5. The physical parameters used in the simulations are provided in Table 1. Concerning with the mass-conservation error (Eq. (35)), all cases display relatively small variations. The algebraic VOF method exhibits the largest errors, independently of the convective scheme used, whereas the mass-conservation error of the geometric VOF, which is also independent of the convective scheme, is in agreement with the results provided by the Basilisk solver. In this case, the mass transfer error between the phases is reduced by an order of magnitude in comparison with FC 1. And, again, the geometric VOF displays a smaller error with respect to the algebraic VOF.

In terms of total energy, all methods display a decrease until $t = 3$ [s], with the TVD schemes exhibiting the highest decay rate, slightly higher than Basilisk. After $t = 3$ [s], the total energy gradually approaches a constant value. At the end of the simulations,

the solutions obtained with the geometric VOF overlap with the Basilisk solutions, and are characterized by the highest dissipation. Among the three simulations based on the algebraic VOF, the highest dissipation is associated with the TVD scheme, the lowest with the MAC scheme, with the HYB scheme lying in between. The time histories of kinetic energy (Fig. 5d) are characterized by an initial rise up to a first peak value. Once the lighter fluid reaches the upper part of the box, it bounces back and then accelerates again attaining a second peak value. At that time instant the different methods display the largest differences, with highest kinetic energy reached by the simulations performed with the algebraic VOF in combination with the MAC scheme, followed by that obtained by the HYB scheme. Due to the presence of viscosity, the fluid motion gradually ceases, and all solutions converge towards the same value, close to zero, at the end of the simulations. The potential energy (Fig. 5e) shows no significant changes in the results obtained from different convective schemes for the geometric VOF. However, it is noteworthy that the algebraic VOF method slightly deviates from the results obtained from the geometric method. This discrepancy may be due to the mass transfer error between the two phases highlighted previously in the algebraic VOF method.

When performing simulations of the Navier-Stokes equations, accurate reproduction of viscous effects with low artificial dissipation is essential for a good numerical scheme. The artificial dissipation of the numerical scheme, referred to as $E_a(t)$, is estimated from equation (41), and reported in Fig. 5f. The results clearly indicate that the TVD scheme introduces the highest artificial dissipation, whereas the MAC schemes yield the least. The HYB scheme lies in between, offering a satisfactory compromise among mass conservation, stability, and limited artificial dissipation. Both the MAC and the HYB schemes perform better than Basilisk solver in this respect, regardless of the scheme used for the transport of the VOF function.

In Fig. 6 and Fig. 7, the $C = 0.5$ iso-surfaces and volume fractions obtained by using different advection schemes and interface approaches at times $t = 1.5 \, [s]$ and $t = 8.0 \, [s]$, respectively, are depicted. The corresponding solutions obtained by using the Basilisk solver are also provided for comparison. When analyzing the solutions shown in Fig. 6, one will note that the density distribution provided by the algebraic VOF is much sharper than for FC1 at the same time, which confirms that the surface tension acts by forcing the immiscibility of the two fluids. The shapes of the interface obtained by the algebraic VOF when using the MAC and the HYB schemes are quite similar, matching the general features of the Basilisk solution. Instead, the use of the TVD scheme introduces additional dissipation, resulting in a noticeable difference in the upper part of the interface compared to the other solutions. As a consequence of the introduction of surface tension, much closer agreement between the algebraic and geometric VOF is observed. The immiscibility of the two fluids, which is now forced by the introduction of surface tension effects, make the use of the VOF approach more appropriate and consistent with the physics.

The effect of the immiscibility of the two fluids becomes even more evident in the solutions at time $t = 8.0 \, [s]$. By comparing the results shown in Fig. 7b-d with the corresponding solutions in Fig. 4b-d, it is evident that the algebraic VOF now exhibits an interface shape that is in perfect agreement with all other solutions. At this time, the solution is approaching a stationary state with the lighter fluid located within a layer occupying the upper part of the box. As a result, no substantial differences are found when varying the VOF algorithm or the convective scheme.

The above results show that in the case of immiscible fluids the VOF model works appropriately, regardless of the interface transport model. More important, the presence of surface tension allows the algebraic VOF to overcome some of its limitations, thus matching the results of geometric VOF. This is also a confirmation of the effectiveness and correctness of the surface tension model.

6. Grid sensitivity analysis

The results in the previous sections were obtained by using a rather coarse discretization. In order to examine the convergence properties of the numerical schemes, the results of numerical simulations of FC2 with grid sizes of $N = 32^3, 64^3, 128^3$ using the HYB scheme are presented. Corresponding results obtained with the Basilisk solver are also shown for comparison. In Fig. 8, the time histories of the energy, viscous dissipation and artificial dissipation are shown at various grid resolutions. The total and kinetic energy plots indicate that differences diminish with grid refinement. As the grid resolution increases, the viscous dissipation, displayed in Fig. 8.c, also increases, especially the first peak. This is because the finer grids can resolve better the smallest scales governing the dissipative processes.

The artificial dissipation, estimated as in equation (41), is shown in Fig. 8.d and, as expected, it decreases with increasing the grid resolution. Notably, the use of the interface sensor confines the dissipation associated with the use of TVD schemes within a narrow region, whereas the energy-preserving MAC scheme is applied to the rest of the fluid domain. As a result, it exhibits significantly lower artificial dissipation compared to the benchmark Basilisk solver. These findings demonstrate the importance of grid resolution in accurately capturing dissipative processes and reducing artificial dissipation. The use of the interface sensor with the HYB scheme offers a favorable compromise between accuracy and computational efficiency, resulting in improved performance compared to the reference solver.

A comparison of the computed interface shapes at $t = 2 \, [s]$ is provided in Fig. 9. The figures suggest that changes in the interface shape are mainly related to the smaller structures, such as bubbles and ligaments, highlighting difficulties encountered in achieving grid convergence. In fact, grid refinement does not necessarily yield precise convergence, as the finest details are inherently different from mesh to mesh. This is due to two reasons. First, in highly nonlinear problems as the one under scrutiny, grid convergence can only be achieved in statistical sense, as the complex interactions between different scales and the nonlinear nature of multiphase flows make it challenging to achieve perfect convergence on a single grid resolution. Second, multiphase flows are characterized by a wide range of scales, from macroscopic to microscopic, which make it impossible, at least with current computational resources, to resolve all scales at the level of the surface microlayer. As a result, some details are always lost or misrepresented, even at extremely fine grid resolutions.
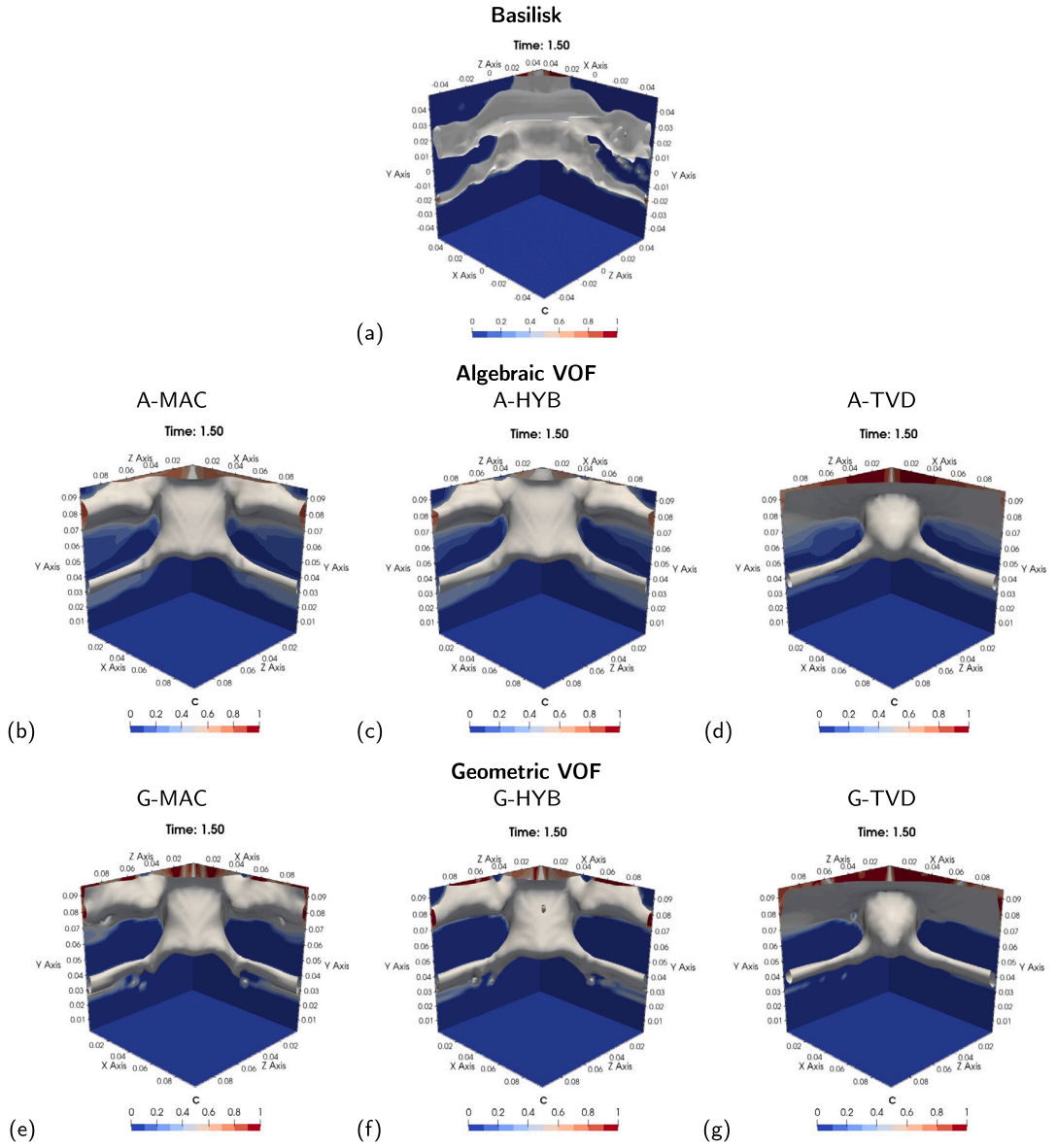
Fig. 6. Flow Case 2: numerical results at $t = 1.5$ [s], obtained by using algebraic (b, c, d) and geometric (e, f, g) VOF with different discretization schemes of convective terms: MAC (b, e), HYB (c, f), TVD (d, g), and Basilisk solver (a). Colored contours of the volume fraction (C) are shown in the coordinate planes, and the $C = 0.5$ iso-surface is shown in grey.

7. Surface tension contribution to the energy balance

In the above discussions, the work done by surface tension forces has been neglected, as in the reference study of Estivalezes et al. [12]. However, it is known that the contribution of surface tension to the energy balance can be not negligible, particularly when a significant fragmentation of the interface occurs.

The work done by surface tension (E_s) can be estimated in two different ways. One way is to compute the energy content associated with surface tension as the product of the surface tension coefficient by the area of the $C = 0.5$ iso-surface, namely

$$E_{s_S}(t) = \sigma S, \tag{42}$$

where S is the surface area of the interface. Another way is to integrate in time the power exerted by the surface tension forces starting from ts contribution in the momentum equation, upon scalar multiplication by $\mathbf{u}$, i.e.

$$E_{s_I}(t) = \sigma \int_t \mathrm{d}t \int_V \mathbf{u} \cdot \mathbf{f}_\sigma \mathrm{d}V, \tag{43}$$
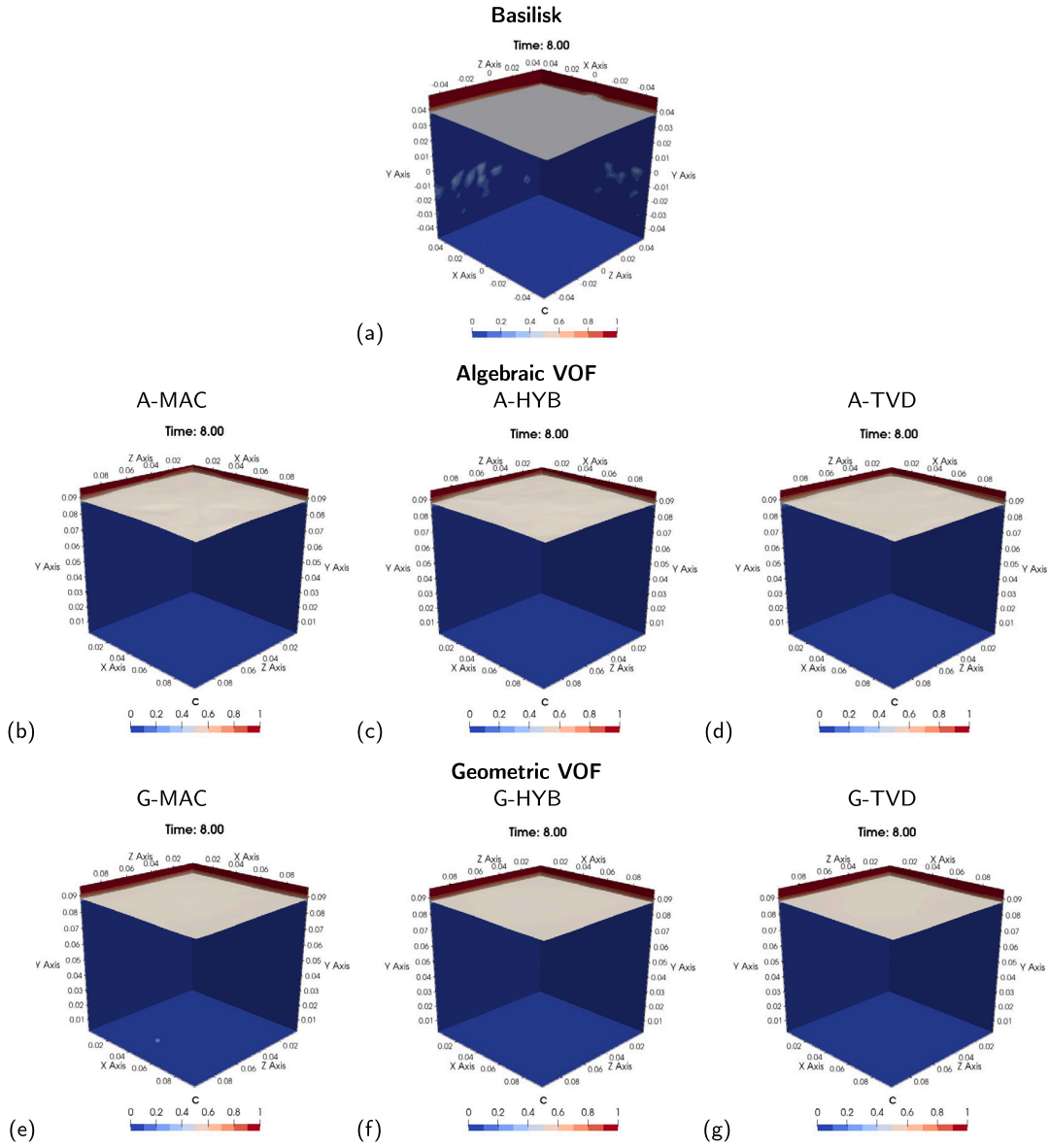
Fig. 7. Flow Case 2: numerical results at $t = 8$ [s], obtained by using algebraic (b, c, d) and geometric (e, f, g) VOF with different discretization schemes of convective terms: MAC (b, e), HYB (c, f), TVD (d, g), and Basilisk solver (a). Colored contours of the volume fraction (C) are shown in the coordinate planes, and the $C = 0.5$ iso-surface is shown in grey.

where $\mathbf{f}_\sigma$ is the local surface tension force. The two different estimates are reported in Fig. 10, for various grid resolutions, exhibiting remarkably different behaviors. The time histories shown in Fig. 10.a seem coherent with the interface configuration as the initial and final values are proportional to the different the interface area at the beginning and at the end of the simulation. In the early stages all meshes yield the same trend whereas, when the interface fragmentation starts, the simulation with lower resolution underestimates the maximum of the energy. Nevertheless, all resolutions approach the same value at the end of the simulation. The surface tension energy estimated from the integration in time of the power of surface tension (Fig. 10.b) is rather similar to that estimated from the interface area at the beginning, but it deviates substantially after the peak energy is attained. The reason for such a deviation is clarified in the following.

The above results indicate that neglecting the surface tension contribution in the analysis of the energy budget might lead to wrong estimates of the artificial dissipation of the different schemes, particularly during the phases when significant fragmentation of the interface takes place. This is particularly evident in Fig. 10.c, where artificial dissipation is estimated from the interface area. In order to highlight changes, the distributions obtained without accounting for surface tension are also shown. The comparison clearly indicates that accounting for the surface tension contribution, the estimated artificial dissipation is reduced.
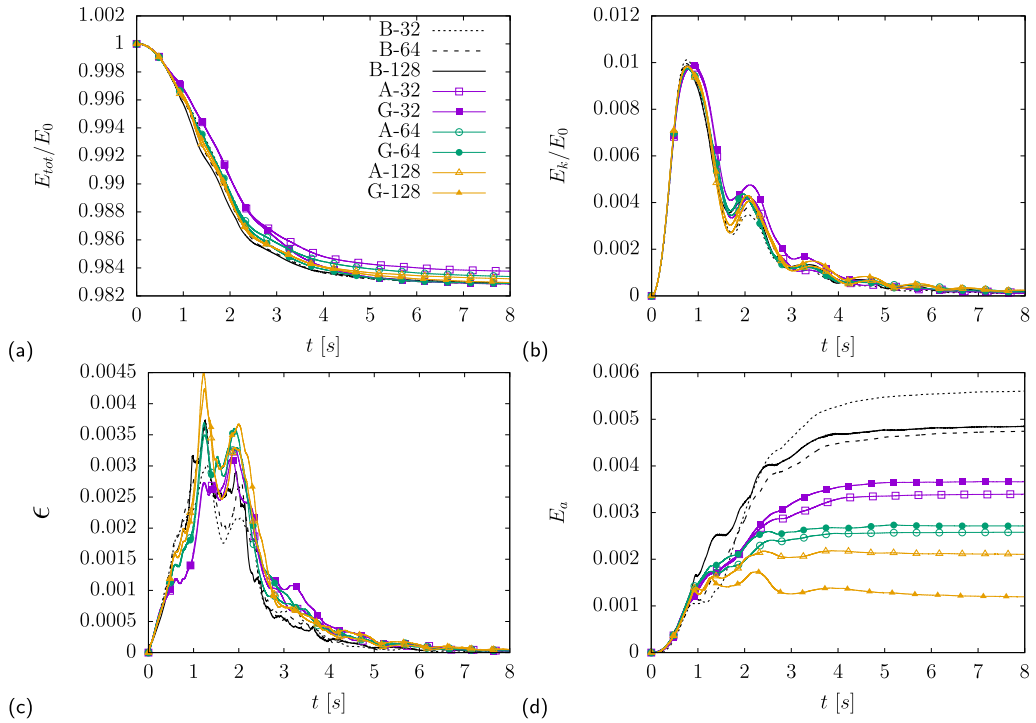
Fig. 8. Grid sensitivity study: comparison of total energy (a), kinetic energy (b), viscous dissipation (c), and artificial dissipation (d) versus time for FC2 simulations; using interface sensor (HYB) with algebraic VOF (open symbols), geometric VOF (solid symbol) and Basilisk (solid/dashed black line). Various grid resolutions are reported: $N = 32^3$ (purple), $N = 64^3$ (green), $N = 128^3$ (yellow).

Even more significant for the quantification of artificial dissipation is the comparison outlined in Fig. 10.d, where the surface tension energy is derived from the integral of the power exerted by surface tension forces in the momentum equation. In this case the reduction of the artificial dissipation is even more significant. This result does not necessarily imply that the surface tension energy evaluated as the time integral of the power of surface tension forces is more accurate. Rather, it suggests that a significant portion of the error in the energy balance arises from the numerical model used for surface tension. In this respect, it is argued that the estimate of the surface tension energy based on the time integral of the surface tension power is not always able to account for the positive work done by surface tension when small bubbles shrink or disappear, releasing their associated energy.

In order to prove this conjecture, in Fig. 11 the surface tension energy evaluated from the area of the interface and the time integral of the power exerted by surface tension forces as computed on the finest mesh, is shown for both geometric and algebraic VOF. The time histories of the number of bubbles are also reported.

The two estimates are nearly overlapping in the early stages when the area of the interface, and thus the surface tension energy based on Eq. (42), increases. After the peak, when the area of the interface diminishes, the differences between the two estimates become rather large. In particular, the estimate based on the time integral of the power of surface tension forces does not decrease as it should. It seems like the model is not able to capture the positive work done by surface tension when the small bubbles shrink and progressively disappear, merging with the main interface. This is particularly evident in the case of the algebraic model, shown in Fig. 11.b, where the two estimates are nearly parallel starting from time $t = 3$ [s] when most bubbles disappear. In order to better highlight this aspect, the time history of the estimate based on the time integral of the power is shifted vertically, displaying, for both the geometric and algebraic VOF, very good overlapping with the estimate based on the area of the interface. Similar considerations hold for the geometric VOF, shown in Fig. 11.a, although the number of bubbles is much higher and the reduction rate is much more gentle compared to the algebraic VOF. As shown in Fig. 11.c.d, even at the end of the simulation, the final configuration of the interface in the case of geometric VOF displays many tiny bubbles that have not yet merged with the main interface, not visible in the solution obtained with the algebraic VOF.

The above results indicate that the numerical model used for surface tension, whereas modelling accurately the action on the fluid preventing the mixing of the two fluids, had some limitations in correctly modelling the positive work done by surface tension when the smaller bubbles shrink. This is an important aspect to be accounted for when estimating the artificial dissipation of the numerical model. The results also indicate that the estimate of the surface tension energy based on the area of the interface is clearly more reliable in the analysis of the energy balance.

In order to investigate possible limitations of the surface tension model in correctly predicting the positive work done by the shrinking of the smaller bubbles, a simple two-dimensional test is conducted, in which a circular bubble is forced by an artificial velocity field to expand and to contract radially. Simulations are conducted using three meshes, with $N = 32^2, 64^2, 128^2$ grid points in a $[-1, 1] \times [-1, 1]$ domain, with an initial bubble radius $r_0 = 0.25$. Tests have been conducted by using the algebraic VOF. Additionally,
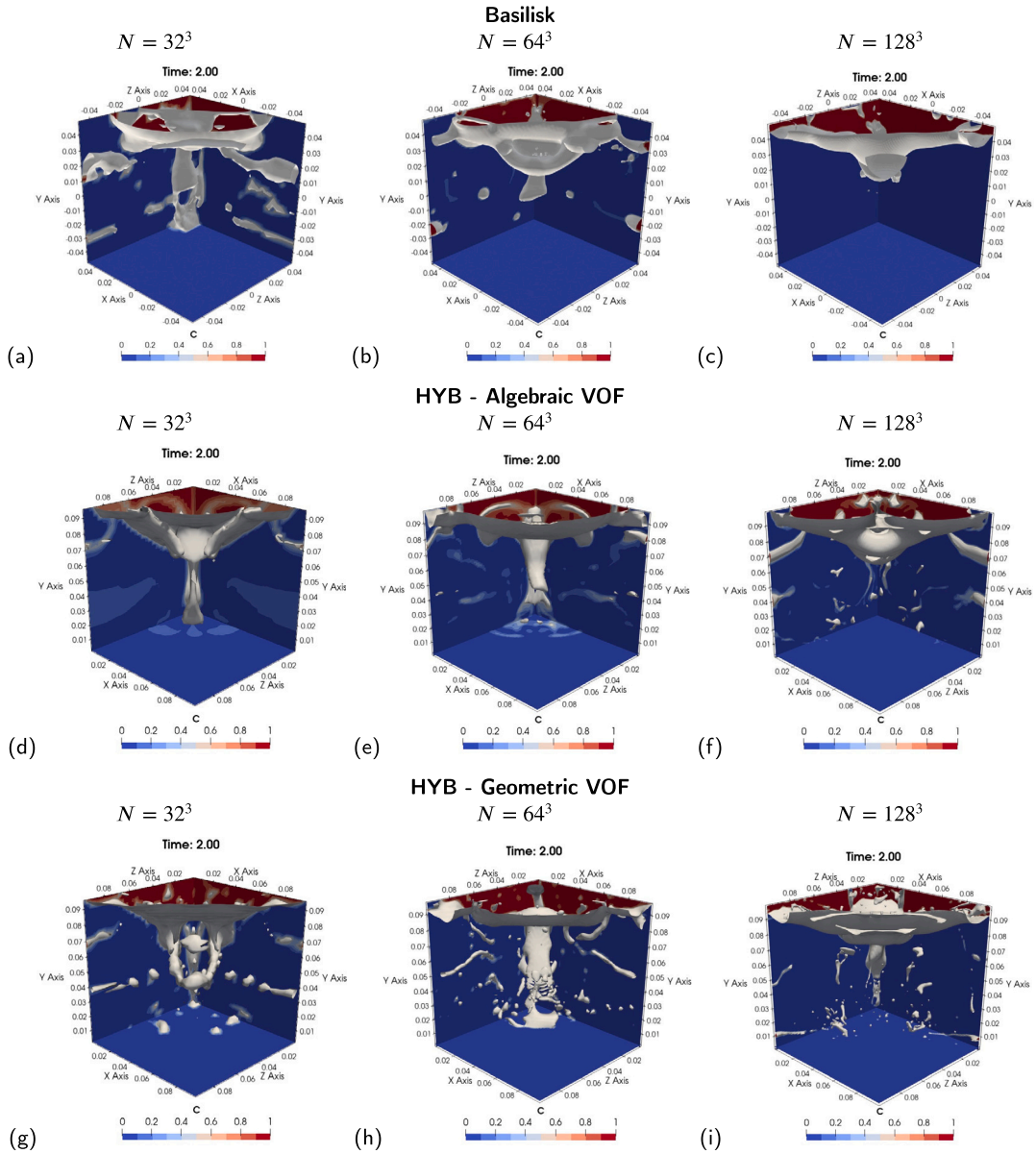
Fig. 9. Flow Case 2, $t = 2.0$: comparison of numerical results obtained with the using the HYB scheme with algebraic (d, e, f) and geometric (g, h, i) VOF, with the Basilisk solver (a, b, c), at various grid resolutions. Colored contours of the volume fraction (C) are shown in the coordinate planes, and the $C = 0.5$ iso-surface is shown in grey.

two different approaches to model surface tension have been employed, i.e. the CSF/HF, the same used for FC1 and FC2, and the continuous surface stress method (CSS), but no noticeable differences have been found in the results, despite the fact that CSS is rarely used with the VOF method because it is affected by a high generation of spurious currents [35]. The estimated surface tension energy is shown in Fig. 12, where negative values indicate that surface tension returns energy to the fluid. Whereas the estimate based on the interface area is independent of the grid resolution, the estimate based on the integral of the power of the surface tension forces appears to underestimate the energy returned to the fluid when the bubble shrinks if the grid is too coarse compared to the bubble size. These results further support the hypothesis that limitations in the numerical model used for surface tension are responsible for a non-negligible portion of the unbalance in the energy budget, and thus contribute to the artificial dissipation of the numerical model.

8. Conclusions

In this study a careful validation and verification of numerical schemes and models used for the simulation of complex multiphase flows has been conducted, putting particular emphasis on the dynamics of the interface between two fluids. To this aim, a test case
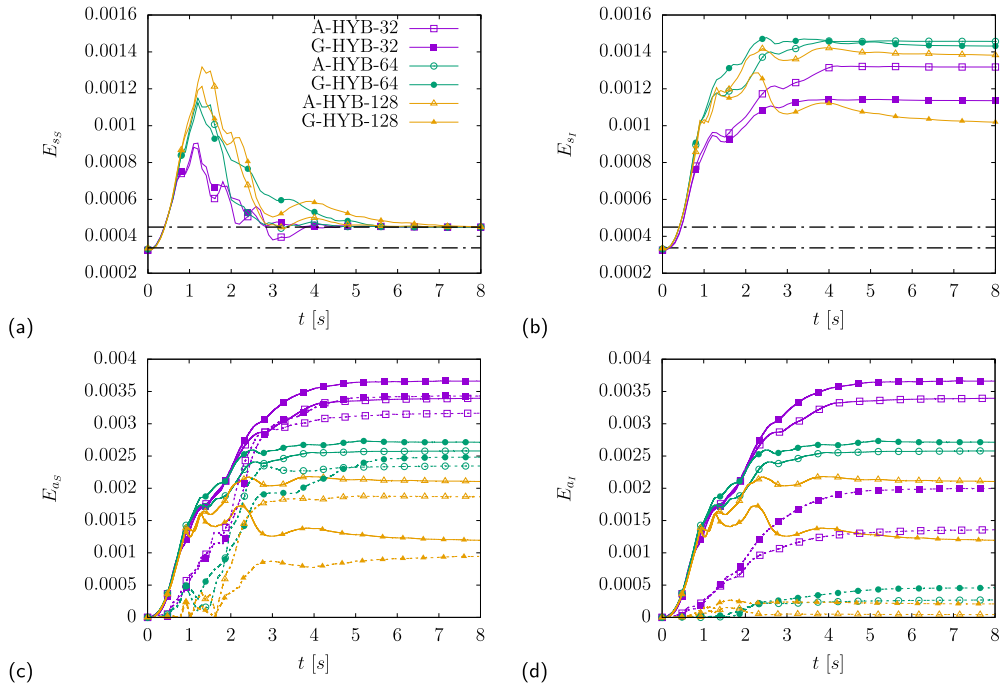
Fig. 10. Time histories of the surface tension energy estimated from Eq. (42), E_{sS} (a), and eq. (43), E_{sI} (b); the two dash-dotted lines in (a) and (b) represent the surface tension energy corresponding to the initial and final values of the area of the fluid interface. Time histories of the artificial dissipation computed starting from E_{sS} (c), and from E_{sI} (d). Solutions computed by using the hybrid approach (HYB) with algebraic VOF are identified by open symbols, whereas the filled symbols are used for the geometric VOF. The results are reported for different mesh resolutions, i.e. $N = 32^3$ (purple), $N = 64^3$ (green) and $N = 128^3$ (yellow).
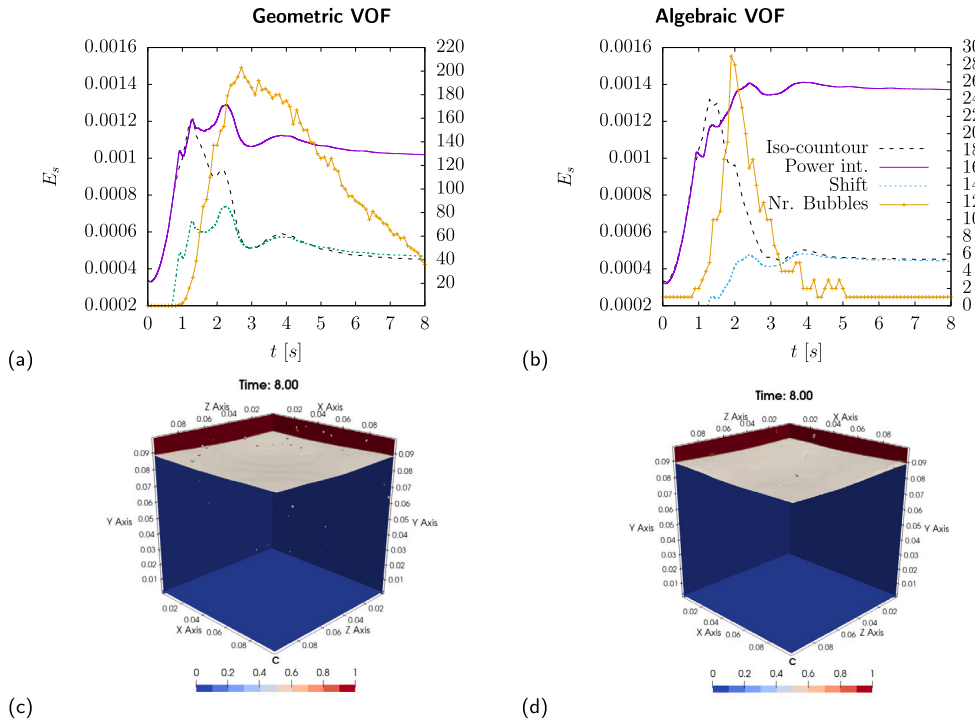

Fig. 11. Comparison of surface tension energy estimated from eq. (42) (dashed line) and eq. (43) (solid line) for the simulations with geometric (a) and algebraic (b) VOF, on a $N = 128^3$ mesh. The time histories of the number of bubbles are also shown in each graph. In order to highlight the agreement of the two different estimates of surface tension energy in the last part of the simulations, a vertical shift is applied to the surface tension energy computed as integral of the power exerted by surface tension forces (dotted lines). In (c) and (d) the $C = 0.5$ iso-surfaces are shown in order to highlight the different number of bubbles/droplets characterizing the final solution of the geometric and algebraic VOF.
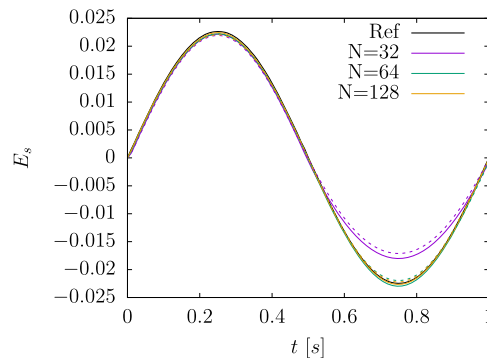
Fig. 12. Time histories of the surface tension energy of a two-dimensional bubble in periodic expansion and contraction, for different grid resolution: $N = 32^2$ (purple), $N = 64^2$ (green), $N = 128^2$ (yellow). The surface tension energy is estimated from the time integral of the surface tension power (eq. (43)) and the results obtained with the CSF/HF method are shown with solid lines while the results from CSS method are shown with dashed lines. The reference curve (dashed black line) is obtained from the analytical value of the area of the interface.

involving the motion of an oil box lying at the bottom corner of a wider cube filled with water has been considered, as proposed by Estivalezes et al. [12].

The study has been focused at the analysis of the role played by the models adopted for the VOF interface tracking and for the discretization of the convective terms in the momentum equation. In order to distinguish the effects connected with the interface transport from those associated with viscosity and surface tension, two flow configurations have been considered, the first one assuming inviscid fluids and no surface tension, the second one including viscosity and surface tension. The first case, although not realistic, has allowed to highlight the impact of the discretization of convective terms on the numerical dissipation, whereas the second flow case has been used to investigate deeper the role played by the surface tension model and the interface dynamics.

It has been found that the energy-preserving, centered scheme, MAC combined with the algebraic VOF model is the best in terms of energy conservation. The geometric VOF, even if used in combination with the MAC scheme, improves the sharpness of the density jump, however at the cost of introducing some artificial dissipation. On the other hand, the MAC scheme has some limitation in terms of robustness, particularly near the interface. For this reason, a hybrid scheme (HYB) has been proposed here which make use of TVD schemes only in a narrow region about the interface, and the MAC scheme elsewhere. As such, the model is much more robust but limits the region where artificial dissipation is introduced.

Particular attention has been paid to the verification of the surface tension model and to the estimate of its contribution to the energy balance. By comparing the results obtained for the two flow configurations, it is found that, when the algebraic VOF is used in combination with the MAC or with the HYB schemes, the introduction of surface tension is able to correct some limitations of the numerical model and to enforce correctly the immiscibility of the two fluids. Furthermore, a detailed analysis of the contribution of the surface tension to the energy balance has been conducted. Aside from its specific amount, accounting for the surface tension energy yields a more accurate estimate of the artificial dissipation of the different schemes. It is found that the most accurate way to determine the effect of surface tension is through the area of the interface. By comparing this estimate with that derived from the time integral of the power exerted on the momentum equation it is observed that the surface tension model is unable to capture correctly the positive work done by surface tension forces when the poorly resolved bubbles shrinks or disappear. The positive work which is not resolved then contributes to overestimating the artificial dissipation of the numerical model.

CRediT authorship contribution statement

Simone Di Giorgio: Conceptualization, Data curation, Methodology, Software, Visualization, Writing – original draft, Writing – review & editing. **Sergio Pirozzoli:** Supervision, Writing – original draft, Writing – review & editing. **Alessandro Iafrati:** Funding acquisition, Project administration, Resources, Supervision, Writing – original draft, Writing – review & editing.

Declaration of competing interest

The authors declare that they have no known competing financial interests or personal relationships that could have appeared to influence the work reported in this paper.

Data availability

Data will be made available on request.

References

[1] N. Ashgriz, J. Poo, Coalescence and separation in binary collisions of liquid drops, J. Fluid Mech. 221 (1990) 183–204.

[2] A. Benkenida, J. Magnaudet, A method for the simulation of two-phase flows without interface reconstruction; Une methode de simulation d'ecoulements diphasiques sans reconstruction d'interfaces, C. R. Acad. Sci., Ser. IIb, Mec. Phys. Astron. (2000).

[3] J.U. Brackbill, D.B. Kothe, C. Zemach, A continuum method for modeling surface tension, J. Comput. Phys. 100 (1992) 335–354, https://doi.org/10.1016/0021-9991(92)90240-Y.

[4] A.J. Chorin, Numerical solution of the Navier-Stokes equations, Math. Comput. 22 (1968) 745–762, https://doi.org/10.1090/S0025-5718-1968-0242392-2.

[5] S.J. Cummins, M.M. Francois, D.B. Kothe, Estimating curvature from volume fractions, Comput. Struct. 83 (2005) 425–434, https://doi.org/10.1016/j.compstruc.2004.08.017.

[6] L. Deike, W.K. Melville, S. Popinet, Air entrainment and bubble statistics in breaking waves, J. Fluid Mech. 801 (2016) 91–129.

[7] J. Delteil, S. Vincent, A. Erriguible, P. Subra-Paternault, Numerical investigations in Rayleigh breakup of round liquid jets with VOF methods, Comput. Fluids 50 (2011) 10–23.

[8] S. Di Giorgio, S. Pirozzoli, A. Iafrati, On coherent vortical structures in wave breaking, J. Fluid Mech. 947 (2022) A44.

[9] H. Ding, C. Shu, K. Yeo, D. Xu, Development of least-square-based two-dimensional finite-difference schemes and their application to simulate natural convection in a cavity, Comput. Fluids 33 (2004) 137–154, https://doi.org/10.1016/S0045-7930(03)00036-7, https://www.sciencedirect.com/science/article/pii/S0045793003000367.

[10] J. Eggers, E. Villermaux, Physics of Liquid Jets, Reports on Progress in Physics, vol. 71, 2008, p. 036601.

[11] D. Enright, R. Fedkiw, J. Ferziger, I. Mitchell, A hybrid particle level set method for improved interface capturing, J. Comput. Phys. 183 (2002) 83–116.

[12] J.L. Estivalezes, W. Aniszewski, F. Auguste, Y. Ling, L. Osmar, J.P. Caltagirone, L. Chirco, A. Pedrono, S. Popinet, A. Berlemont, et al., A phase inversion benchmark for multiscale multiphase flows, J. Comput. Phys. 450 (2022) 110810.

[13] R.D. Falgout, U.M. Yang, hypre: A library of high performance preconditioners, pp. 632–641, https://doi.org/10.1007/3-540-47789-6_66, http://link.springer.com/10.1007/3-540-47789-6_66, 2002.

[14] M.M. Francois, S.J. Cummins, E.D. Dendy, D.B. Kothe, J.M. Sicilian, M.W. Williams, A balanced-force algorithm for continuous and sharp interfacial surface tension models within a volume tracking framework, J. Comput. Phys. 213 (2006) 141–173, https://doi.org/10.1016/j.jcp.2005.08.004.

[15] L. Gilman, E. Baglietto, A self-consistent, physics-based boiling heat transfer modeling framework for use in computational fluid dynamics, Int. J. Multiph. Flow 95 (2017) 35–53.

[16] R. Goldman, Curvature formulas for implicit curves and surfaces, Comput. Aided Geom. Des. 22 (2005) 632–658, https://doi.org/10.1016/j.cagd.2005.06.005.

[17] F.H. Harlow, J.E. Welch, Numerical calculation of time-dependent viscous incompressible flow of fluid with free surface, Phys. Fluids 8 (1965) 2182–2189.

[18] J. Hernández, J. López, P. Gómez, C. Zanzi, F. Faura, A new volume of fluid method in three dimensions—part I: multidimensional advection method with face-matched flux polyhedra, Int. J. Numer. Methods Fluids (2008).

[19] C.W. Hirt, B.D. Nichols, Volume of fluid (VOF) method for the dynamics of free boundaries, J. Comput. Phys. 39 (1981) 201–225.

[20] D. Jamet, O. Lebaigue, H. Lemonnier, Test-cases for interface tracking methods, http://test.interface.free.fr/, 2004.

[21] C. Josserand, S.T. Thoroddsen, Drop impact on a solid surface, Annu. Rev. Fluid Mech. 48 (2016) 365–391.

[22] J.C. Lasheras, E. Hopfinger, Liquid jet instability and atomization in a coaxial gas stream, Annu. Rev. Fluid Mech. 32 (2000) 275–308.

[23] Y. Ling, D. Fuster, G. Tryggvason, S. Zaleski, A two-phase mixing layer between parallel gas and liquid streams: multiphase turbulence statistics and influence of interfacial instability, J. Fluid Mech. 859 (2019) 268–307.

[24] J. López, J. Hernández, On reducing interface curvature computation errors in the height function technique, J. Comput. Phys. 229 (2010) 4855–4868, https://doi.org/10.1016/j.jcp.2010.03.032.

[25] J. Lu, G. Tryggvason, Direct numerical simulations of multifluid flows in a vertical channel undergoing topology changes, Phys. Rev. Fluids 3 (2018) 084401.

[26] P. Orlandi, Fluid Flow Phenomena: a Numerical Toolkit, vol. 55, Springer Science & Business Media, 2012.

[27] S. Osher, R.P. Fedkiw, Level set methods: an overview and some recent results, J. Comput. Phys. 169 (2001) 463–502.

[28] S. Pirozzoli, Numerical methods for high-speed flows, Annu. Rev. Fluid Mech. 43 (2011) 163–194.

[29] S. Pirozzoli, S. Di Giorgio, A. Iafrati, On algebraic TVD-VOF methods for tracking material interfaces, Comput. Fluids 189 (2019) 73–81.

[30] S. Popinet, An accurate adaptive solver for surface-tension-driven interfacial flows, J. Comput. Phys. 228 (2009) 5838–5866.

[31] S. Popinet, Basilisk flow solver, http://basilisk.fr. (Accessed 2 October 2018), 2013.

[32] A. Prosperetti, Motion of two superposed viscous fluids, Phys. Fluids 24 (1981) 1217–1223.

[33] W. Rider, D. Kothe, Reconstructing volume tracking, J. Comput. Phys. 141 (1998) 112–152.

[34] S. Tanguy, A. Berlemont, Application of a level set method for simulation of droplet collisions, Int. J. Multiph. Flow 31 (2005) 1015–1035.

[35] G. Tryggvason, R. Scardovelli, S. Zaleski, Direct Numerical Simulations of Gas-Liquid Multiphase Flows, Cambridge University Press, 2011.

[36] G.D. Weymouth, D.K.P. Yue, Conservative volume-of-fluid method for free-surface simulations on Cartesian-grids, J. Comput. Phys. 229 (2010) 2853–2865.

[37] S. Zalesak, Fully multidimensional flux-corrected transport algorithms for fluids, J. Comput. Phys. 31 (1979) 335–362.